Research Article | Vol. 30, No. 14 / 4 Jul 2022 / Optics Express 25817
Optics EXPRESS

Fabrication error tolerant broadband mode converters and their working principles

MD MAHADI MASNAD,[1,*] GUOWU ZHANG,[1] DAN-XIA XU,[2] YURI GRINBERG,[3] AND ODILE LIBOIRON-LADOUCEUR[1]

[1]Electrical and Computer Engineering Department, McGill University, Montreal, Canada
[2]Advanced Electronics and Photonics Research Center, National Research Council Canada, Ottawa, Canada
[3]Digital Technologies Research Center, National Research Council Canada, Ottawa, Canada
[*]md.masnad@mail.mcgill.ca

Abstract: Computational inverse design techniques have shown potential to become reliable means for designing compact nanophotonic devices without compromising the performance. Much effort has been made to reduce the computation cost involved in the optimization process and obtain final designs that are robust to fabrication imperfections. In this work, we experimentally demonstrate TE0-TE1 and TE1-TE3 mode converters (MCs) on the silicon-on-insulator platform designed using the computationally efficient shape optimization method. These MCs have mode conversion efficiencies above 95%, and the insertion loss ranges from 0.3 dB to 1 dB over a wavelength span of 80 nm ranging from 1.5 μm to 1.58 μm. Maximum modal crosstalk found experimentally in the C-band is -19 dB. The conversion efficiency drops at most by 2.2% at 1.55 μm for 10 nm over/under etch, implying good robustness to dimensional variations. We present the mode conversion mechanism of these MCs by studying the simulated electromagnetic field patterns and validate with supportive data. We also demonstrate their performance in the time domain with a 28 Gbps OOK and a 20 GBaud PAM-4 payload transmissions, which supports their utility for high throughput data communications. The open eye diagrams exhibit Q-factors of 8 dB.

1. Introduction

Combined with wavelength-division multiplexing and polarization-division multiplexing, utilizing orthogonal spatial optical modes in multimode waveguides further increases on-chip data processing rate within limited chip area [1,2]. Since the fundamental mode is usually coupled most efficiently to the waveguide from the fiber, on-chip mode conversion of the fundamental mode to higher order modes requires mode converters (MCs) [2,3]. MCs also have important applications in coupling between various types of waveguides [4,5] as different waveguides are suitable for different functionalities, such as photonic crystal waveguides for slow light applications [3,6] and metal-insulator waveguides for surface plasmon resonance [7,8], to name a few. Mode converters designed in traditional approaches, such as asymmetric directional coupler [9] and Bragg grating [5], usually have large footprints. MCs designed using micro-ring resonators encompass small footprint but suffer from narrow bandwidth [10]. For high performance and compact designs, various inverse design methods demonstrate significant advantages over the traditional approaches by tuning a large number of design parameters [11–15]. Consequently, computational inverse design of nanophotonic devices received much attention recently in improving the performance of various photonic integrated circuits [16–20]. Mode converters designed using topology optimization, a versatile inverse design method, are compact and have high conversion efficiencies [4,11]. But the disadvantages are possible tiny features in the design area and an additional computation cost for boundary optimization carried out in the binarization step [21]. Moreover, discrete features, typical of topological inverse design

#461979 https://doi.org/10.1364/OE.461979
Journal © 2022 Received 5 May 2022; revised 17 Jun 2022; accepted 20 Jun 2022; published 1 Jul 2022

Optics EXPRESS

methodology, make the device performance sensitive to common fabrication errors such as under and over etches. To mitigate these issues, a novel method called topology optimization with energy constraint has been proposed by our group [16]. It results in devices comparatively more tolerant to fabrication errors by limiting the optical field overlap with the design structure sidewalls. For simple functionalities such as mode conversion, power splitting, etc., this approach remains computationally demanding. Another method known as direct binary search, in which the minimum pixel dimension is kept larger than the allowed minimum feature size, is often used to design photonic devices to perform various mode manipulation operations in silicon photonics [17,18]. But design optimization in this method incurs a significant computation cost. Also experimentally, these devices suffer from lower transmission (in the order of -1 dB to -2.2 dB) and higher crosstalk (at most -8.5 dB). Mode converters are also designed implementing inverse design methods on photonic crystal waveguides. However, such MCs often have either lower conversion efficiency and higher crosstalk [15] or narrower bandwidth [22].

In this work, we report compact broadband mode converters designed using the shape optimization method. A small set of structure boundary points are parameterized, and a gradient-based algorithm changes the shape of the material block in the design area to maximize a defined figure of merit (FOM). This approach does not require any binarization step since the structure is binarized right from the beginning. Consisting of a single silicon block, the optimized designs are readily manufacturable and robust to dimensional variations such as 10 nm under/over etch, which corresponds to ±20 nm waveguide width variation. To demonstrate the scalability, MCs were designed for mutual conversion of different combinations of mode pairs among the first four quasi-transverse electrical (TE) modes (*e.g.*, fundamental TE mode, TE0, to 3rd order mode, TE3). The simulation and experimental results of two MCs, *i.e.*, TE0-TE1 and TE1-TE3, are highlighted here. The measured insertion losses (IL) are below 1 dB over a wavelength span of 80 nm ranging from 1.5 μm to 1.58 μm, and the modal crosstalks (XT) are below -19 dB in the C-band (1.53 to 1.565 μm). We present the mode conversion mechanism of these MCs by studying the simulated electromagnetic field patterns and validate with supportive data. Payload transmissions (28 Gbps On-Off-Keying, OOK, and 20 GBaud 4-level pulse amplitude modulation, PAM-4) have been carried out for time domain characterization, and open eye diagrams are obtained.

2. Design approach

The mode converters are designed for their implementation on a commercial silicon-on-insulator (SOI) platform with a silicon layer thickness of 220 nm and a 2 μm thick buried oxide layer. The top cladding consists of 2.2 μm deposited silicon dioxide (SiO_2). Thus, any point in the design area assumes either of the two material permittivities, ϵ_{Si} = 12.11 and ϵ_{SiO_2} = 2.085 [24]. As a common practice in shape optimization, a device geometry from either an initial guess or a random initialization is needed as the starting structure to begin the optimization. We find that deciding the dimensions and the aspect ratio of the design area is one of the most important contributing factors to the final device performance. While the widths of the input and output (I/O) waveguides depend mostly on the application and the device interface with the rest of the circuit, their positions and spacing directly determine the local and global optima in the design parameter space. Particularly in this work, the mode conversion requires relative phase shifts on the traveling wavefront, which in turn requires a sufficiently long optical path to traverse in the design area. For TE0-TE1 MC, for instance, reducing the device length below 3 μm results in lower CE (at a length of 2.5 μm, CE is approximately 92%) as well as XT worse than -18 dB. Increasing the device length beyond 3.5 μm does not significantly improve the CE, while the XT performance improves by a few decibels. Without designer intervention or manual tuning, inverse design techniques can generally find local optima in the design parameter space with respectable performance [11]. However, utilizing physical intuition in deciding the starting geometry space

Optics EXPRESS

for the optimization lead to computational cost reduction and devices with better performance [23].

As shown in Fig. 1(a), 20 points on the structure boundary are taken as the design parameters. The limited-memory Broyden-Fletcher-Goldfarb-Shano bound-constrained (L-BFGS-B) [25], a quasi-Newton algorithm, is employed to optimize a figure of merit (FOM). The design parameters, *i.e.*, the vertical positions of the boundary points, are updated according to the gradient information from the current iteration and the estimated second-order derivative information of the FOM from the previous iterations. A line search, performed in each iteration, determines the step length. The optimization terminates when the gradient amplitude is smaller than 10^{-5}. In every iteration, a forward and an adjoint simulations are performed to evaluate the field profile and calculate the gradient of the FOM with respect to the permittivity at every pixel in the design area. This gradient is multiplied to the partial derivatives of the permittivity with respect to the design parameters to calculate the gradient of the FOM with respect to the design parameters. The FOM is defined as the average mode conversion efficiency at 11 equally spaced wavelength points across the bandwidth from the input mode to the desired output mode for broadband performance. The conversion efficiency (CE) is defined here as the ratio of the power transmitted into the specified mode in the output waveguide ($P_{out,T}$) and the power in the input mode ($P_{in,S}$).

$$CE = P_{out,T}/P_{in,S} \tag{1}$$

$$FOM = \frac{1}{n}\sum_{i=-(n-1)/2}^{(n-1)/2} CE\left(\lambda_0 + i\frac{\Delta\lambda}{n-1}\right), \tag{2}$$

where $n = 11$, $\lambda_0 = 1.5$ μm, and $\Delta\lambda = 100$ nm. Here the modal crosstalk is defined as the optical power coupling to any other guided mode except for the target mode. To quantify the XT, the ratio of the optical power in the undesired mode ($P_{out,U}$) and the total input power is calculated in dB unit.

$$XT = 10log_{10}(P_{out,U}/P_{in,S}) \tag{3}$$

Since maximizing the CE alone results in low crosstalk MCs, modal crosstalk is not adopted in the FOM in this work. The designs are optimized through 2D simulations first. If the FOM exceeds 90%, the 2D optimized design is used as the starting structure for 3D optimization. This is a time efficient approach since a computer with a processor having four cores (Core i7-3770 CPU @ 3.40 GHz) takes around 24 minutes to perform one iteration in 3D optimization whereas 18 iterations in 2D can be executed in the same amount of time. Most MCs in this work converge to the final designs within 50 iterations through 2D simulations and then around 29 iterations on average in 3D optimization. In the 2D optimization, the effective index method is used where a refractive index of 2.85 is used for quasi-transverse electrical (quasi-TE) modes. The simulations are performed using Ansys Lumerical Mode and FDTD solvers [26], and the optimizations are done using an open-source package, LumOpt, along with the scipy package, an open-source Python library used for scientific and technical computing. The design approach is similar to the one reported by C. M. Lalau-Keraly *et. al.* in [12]. The code provided in the "Lumerical support" [27] is used as a template, which can be directly used to design symmetric devices with symmetric electromagnetic field distributions with respect to the propagation axis. The code is modified to move all the parameter points up and down independently to incorporate asymmetry in the design structure. Additionally, the "cubic"-type interpolation used in the template often results in self-intersecting polygon boundaries, which is a problem because the resulting structures are not realistic designs. In this work, this part is replaced with a Gaussian smoothing filter which is convolved with linearly interpolated boundary points defining the design structure. The mesh size for the simulations is set to 20 nm along all axes providing sufficiently fine resolution to obtain reliable results. All the optical modes in this work are quasi-TE modes in the waveguides

Optics EXPRESS

confined in two dimensions, but for ease of discussion in the upcoming sections, we often drop the prefix "quasi" before TE modes.

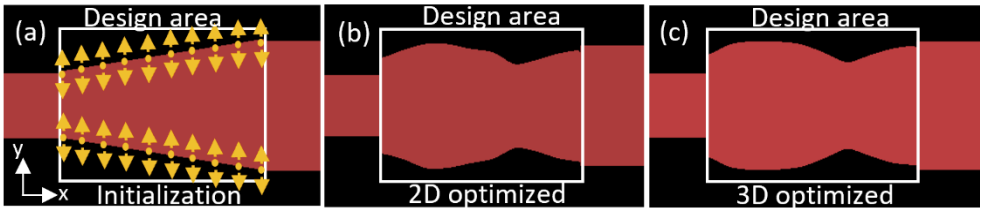

Fig. 1. (a) Initialization of the optimization in 2D simulation, the boundary points on the sidewalls are parameterized, (b) 2D optimized design, which is the starting point for initiating optimization in 3D simulation, (c) 3D optimized design, ready for fabrication.

3. Result and performance analysis

3.1. TE0-TE1 mode converters

To convert the fundamental TE mode into TE1 mode with different I/O waveguide dimensions but aligned with respect to each other (*i.e.*, on the same horizontal axis), out of 97 initializations, we obtained 16 TE0-TE1 mode converters with conversion efficiencies above 95% at 1.55 µm in 3D FDTD simulation. The device lengths vary from 3 µm to 3.6 µm. Three designs were selected for fabrication. To characterize the mode converter under study, we inserted two mode-division (de)multiplexers (MDM) to interface with the single mode input and output waveguides. The MDM is designed using asymmetric directional couplers (DC) [28] to excite TE1 mode from the TE0 mode and also to separate them (demux). This MDM is further optimized and characterized by our research group [29]. The measurement error (or performance variation) of this mode multiplexer is approximately 0.5 dB according to our previous investigation [30]. Figure 2 shows the schematic of the circuit block used for device characterization and how different optical modes are routed. In forward propagation, TE0 mode is sent through the multimode waveguide. The MC converts it to TE1 mode which propagates through the multimode waveguide on the right along with the unconverted optical power remaining in TE0 mode as the crosstalk. The directional coupler separates TE1 mode from the crosstalk utilizing evanescent coupling. The widths of the two arms of the DC are tuned such that effective index of TE1 mode in the wider waveguide matches with that of TE0 mode in the narrower waveguide. Thus, TE1 mode couples to TE0 mode in the single mode waveguide in the upper arm. Similarly, in the reverse propagation, input TE0 mode excites TE1 mode in the multimode waveguide. The MC converts it to TE0 mode and the unconverted optical power in TE1 mode is separated by the DC on the left. By increasing the width of the multimode waveguide, higher order TE modes are excited and also separated by the DCs, used for the characterization of TE1-TE3 MC reported in section 3.2.

Fig. 2. Schematic of the circuit block for device characterization, showing the forward (in green) and reverse (in red) propagation through the TE0-TE1 mode converter.

Figure 3(a) shows an optical microscope image of the circuit block for device characterization. Two grating couplers (GCs), numbered 1 and 6, connected by a 0.5 µm wide single-mode

Optics EXPRESS

waveguide are used to align a 12-channel optical fiber array with the grating couplers connected to the MDM circuit. The MC is placed at the position marked by the blue rectangle. The scanning electron microscope (SEM) image of one MC and its footprint are shown in Fig. 3(b). The mode conversion efficiencies for both directions, calculated in 3D FDTD simulations, are plotted in Fig. 3(d). Simulation predicts the mode conversion efficiencies in both directions are above 95% across a wavelength span of 100 nm from 1.5 µm to 1.6 µm. The spatial electric field amplitude profile of the mode conversion is shown in the inset of Fig. 3(d).

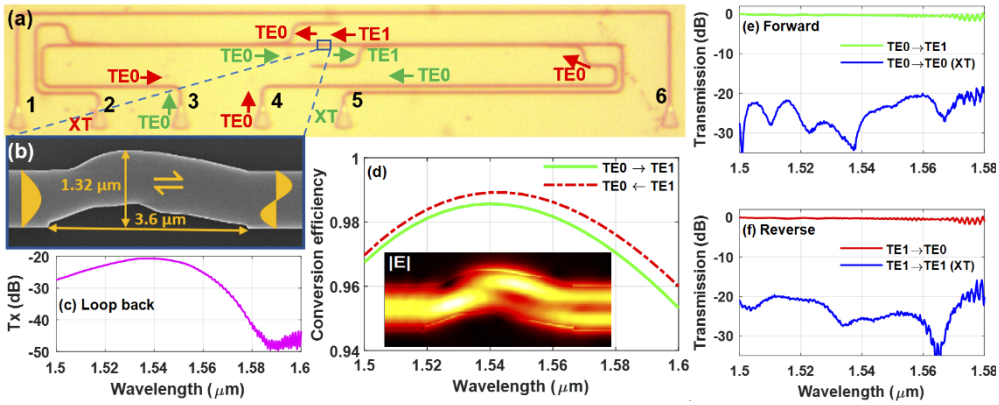

Fig. 3. (a) Optical circuit block used to measure the transmission and crosstalk of TE0-TE1 MCs, also showing the forward (green) and reverse (red) propagation with arrows, (b) SEM image of the TE0-TE1 mode converter, (c) transmission spectrum of the loop-back structure, showing undesired fluctuations at wavelengths longer than 1580 nm. with 19.4 dB insertion loss at 1.54 µm, (d) mode conversion efficiencies, calculated in 3D FDTD simulations, for the forward propagation (TE0 → TE1) and the reverse propagation (TE1 → TE0); inset: spatial electric field amplitude profile, (e) transmission into desired TE1 mode and the modal crosstalk into TE0 mode, (f) transmission into desired TE0 mode and the modal crosstalk into TE1 mode for propagation in the reverse direction.

To measure the transmission spectra, a tunable laser and a power meter with sensitivity of −78 dBm at 1550 nm are used to collect transmission data at a wavelength interval of 0.2 nm between 1.5 µm and 1.6 µm. The laser output is 10 dBm and the combined insertion loss of the polarization controller and connectors is ~1 dB. All continuous wave (CW) measurements are normalized to a loopback structure. To account for any excess loss coming from the asymmetric directional coupler-based MDM, a circuit block like the one shown in Fig. 3(a) is used but without any mode converter. The optical signal is sent through GC-2 and collected from GC-4 for the transmission, while optical modal crosstalk is measured through GC-5, which is below -30 dB across the wavelength range from 1.5 µm to 1.58 µm. Figure 3(c) shows the back-to-back GC insertion loss is 19.4 dB, implying the coupling loss of the grating coupler being 9.7 dB. The corresponding measurement error (or performance variation) for IL of the grating coupler at 1550 nm is approximately 1.2 dB according to the previous publication [31]. The fluctuations in the transmission spectrum, which come from the large back reflection of the GCs, makes the experimental data less reliable at longer wavelengths. Therefore, we do not report the experimental data beyond 1.58 µm, although the MCs are optimized to operate across the bandwidth of 1.5-1.6 µm. The normalized transmission spectra in Fig. 3(e) and 3(f) show an insertion loss of the mode converter below 0.5 dB and a modal crosstalk at most -18 dB for mode conversion in both directions across the wavelength range from 1.5 µm to 1.58 µm.

Optics EXPRESS

3.2. TE1-TE3 mode converters

The next set of MCs we designed are for TE1-TE3 mode conversion. We chose the input and the output waveguides to be 1 μm and 2 μm wide, respectively, placed along the same horizontal axis (*i.e.*, aligned horizontally). The spacing between them was varied from 3.2 μm to 4.2 μm to find an optimum length of the design area. With several random initializations, we obtained three final designs with conversion efficiencies above 97% at 1.55 μm and similar crosstalk performances. The SEM image and performance of one MC are reported in Fig. 4. The optical microscope image of a segment of the tapered directional coupler-based MDM array is shown in Fig. 4(a), which separates (or demultiplexes) four quasi-TE modes into four channels for transmission and crosstalk measurement. The TE1-TE3 mode converter is placed at the left end of the cascaded MDMs. Using a tapered directional coupler, TE1 mode is excited from the fundamental TE mode in the 1 μm wide waveguide on the left of the mode converter. The MC transforms the input mode into TE3 mode, while a small fraction of light couples to lower order modes as crosstalk. The width of the multimode- waveguide is changed at three successive directional couplers such that TE3, TE2, and TE1 modes are separated one by one by the DCs leaving behind TE0 mode as light travels forward. The design structure, shown in Fig. 4(b), encompasses a footprint of 4×2 μm^2. The device boundary evolved to be symmetric with respect to the propagation axis, while the field profile is antisymmetric. Similar to the previous device, this MC is also bidirectional; if the TE1 mode is sent through the narrower waveguide, the device converts it to the TE3 mode which propagates in the wider waveguide, and vice versa. The mode conversion efficiency in both directions is above 95% across a 100 nm wavelength span between 1.5 μm and 1.6 μm. Figure 4(d) and 4(e) show the measured transmission spectra for the forward and reverse propagation. In both directions, the insertion losses are below 1 dB over the full reported bandwidth, and modal crosstalks below -20 dB in the C-band.

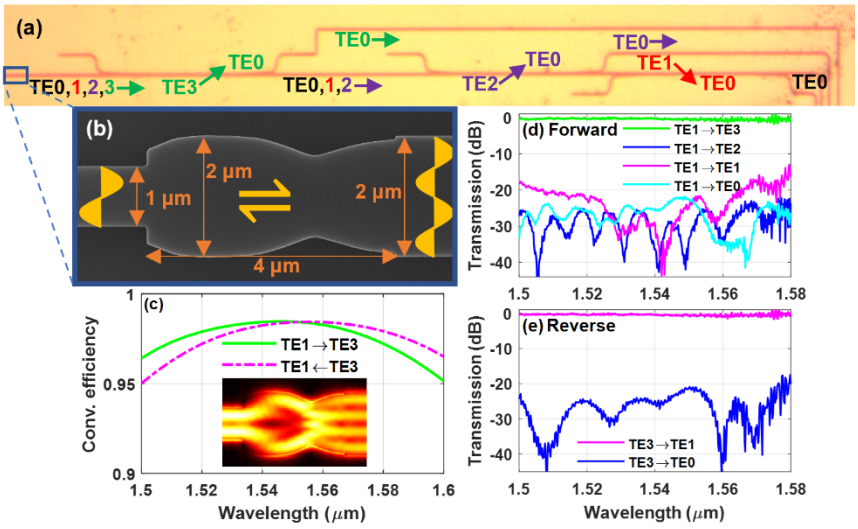

Fig. 4. (a) A segment of the tapered directional coupler-based MDM array to separate four quasi-TE modes and excite higher order modes from the fundamental TE mode, (b) the SEM image of a TE1-TE3 mode converter and its dimensions, (c) mode conversion efficiencies above 95% across the bandwidth, calculated using 3D FDTD simulation in both mode conversion directions; inset: spatial electric field amplitude profile, (d) transmission into desired TE3 mode and the modal crosstalk in lower order TE modes; crosstalk is below -20 dB in C-band, (e) transmission into desired TE1 mode and the modal crosstalk into TE0 mode for propagation in the reverse direction.

Optics EXPRESS

3.3. Robustness to dimensional variations

To investigate the effects of dimensional variations in fabricated devices, we intentionally extended (and shrunk) each of the side walls of the mode converter layout (including the I/O waveguides) by 10 nm to mimic the effect of under (and over) etch. Along with the nominal designs, we also included these variants with intentional extended and shrunk boundaries for fabrication. Figure 5(a) illustrates the design layouts after introducing ±10 nm etch errors; +10 nm refers to extension of each sidewall by 10 nm, resulting in waveguide width expansion of 20 nm to emulate the under etch error, and -10 nm refers to the opposite. Figure 5(b) and 5(c) show how the CE is affected for extended and shrunk boundaries for TE0-TE1 and TE1-TE3 mode converters, respectively, in 3D FDTD simulations. At 1.55 μm wavelength for TE0-TE1 mode converter, CE drops by ~2.2%, and the CE peaks shift in opposite directions. But for the TE1-TE3 converter, the conversion efficiency drops only by 0.6%. Similarly, its CE peaks move away from the central wavelength in opposite directions. The shifts of CE peak wavelength and efficiency drop for the same ±10 nm change for TE1-TE3 mode converter are smaller than those observed for TE0-TE1 mode converters. This can be explained by the relative size of the devices. Compared to the TE0-TE1 mode converter, TE1-TE3 mode converter is large. The same amount of variation of the boundary of TE0-TE1 MC leads to relatively higher changes; thus, larger shifts of CE peak. The experimental results confirm that under-etched MCs are more efficient at longer wavelengths while over-etched MCs at shorter wavelengths, which is predicted in simulation. The transmission and crosstalk spectra for 10 nm under and over etched TE1-TE3 mode converter are plotted in Fig. 5(d) and 5(e). Apparently, under etched TE1-TE3 MC performs better at longer wavelengths, manifested by low insertion loss (0.1 dB at 1.56 μm) and lower crosstalk. On the other hand, over etched MC performs better at shorter wavelengths; transmission drops significantly at longer wavelengths. Across the C-band, all three variants of the MC have transmissions above -0.5 dB and crosstalk below -19.5 dB, indicating its robustness to ±10 nm etch errors. To compare with the mode conversion efficiencies of inverse-designed TE0-TE1 mode exchanger for ±20 nm etch errors reported in [17], we ran additional simulation on our TE0-TE1 mode converter incorporating equal amount of under and over etches. The MC in this work shows ~10% higher mode conversion efficiency than that reported in [17]. The mode conversion efficiencies for ±20

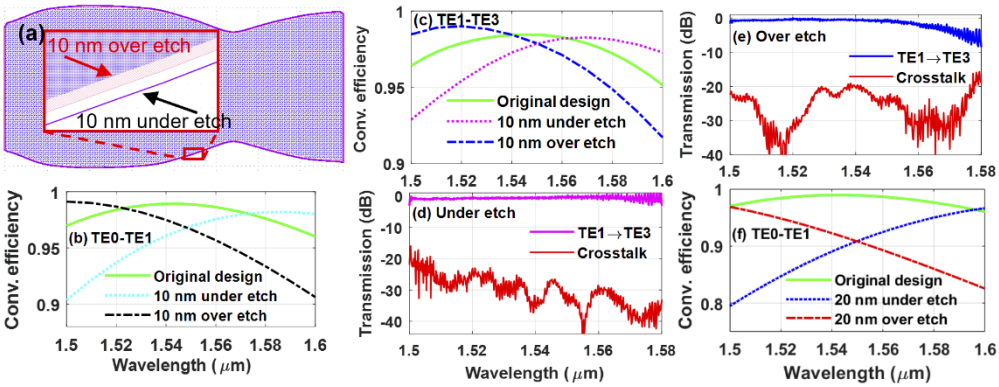

Fig. 5. (a) Layouts of the TE1-TE3 mode converter and its ±10 nm etch variants, overlayed on top of each other, (b) effects of 10 nm under and over etches on the conversion efficiency of TE0-TE1 mode converter in simulation, (c) effects of 10 nm under and over etches on the conversion efficiency of TE1-TE3 mode converter in simulation. Transmission and crosstalk spectra of (d)10 nm under etched and (e) 10 nm over etched TE1-TE3 mode converter, (f) effects of 20 nm under and over etches on the conversion efficiency of TE0-TE1 mode converter in simulation.

Optics EXPRESS

nm etch errors are plotted in Fig. 5(f). Despite 20 nm dimensional variations, the conversion efficiencies remain above 90% at 1.55 μm. Apart from these devices, TE0-TE2 (6.7 μm long) and TE1-TE2 (7.8 μm long) MCs have also been optimized [23] and experimentally characterized, but not discussed here in details because of the space limitation. Table 1 presents a summary of the key performance parameters of the four mode converters in this work along with the MCs reported by other research groups.

Table 1. Performance summary of the MCs in this work and previously reported MCs

Ref.	Mode conversi-on pair	Footprint (μm^2)	Average CE in simulati-on	Decrease in CE at 1.55 μm for ±20 nm width variations	Reported Bandwidth	Maximum IL across the reported bandwidth	Maximum XT measured across the bandwidth
[11]	TE0-TE1	2.4 × 1.6	86.4%	Not reported	Not reported	Not reported	Not reported
[15]	TE0-TE1	6.3 × 3.6	82.0%	Not reported	43 nm	2.0 dB	-12.0 dB
[32,33]	TE0-TE1	18.6 × 2.65	98.6%	Not reported	100 nm	0.4 dB	-21.0 dB
[32,33]	TE2-TE0	19.3 × 4.68	98.8%	Not reported	100 nm	0.5 dB	-18.0 dB
This work	TE0-TE1	3.6 × 1.32	97.7%	0.6%	80 nm	1.0 dB	-18.0 dB
This work	TE1-TE3	4 × 2	97.6%	2.2%	80 nm	0.8 dB	-17.0 dB
This work	TE2-TE0	6.7 × 2.4	95.1%	1.6%	80 nm	1.2 dB	-13.0 dB
This work	TE1-TE2	7.8 × 2.25	98.0%	1.3%	80 nm	0.8 dB	-18.2 dB

3.4. Working mechanism

The working mechanisms of various inverse-designed nanophotonic devices were often deemed nonintuitive/complicated [11,12], and informative discussion is absent in most of the reports on inverse design [15–20]. Here we explain the mode conversion mechanism by analyzing the simulated field patterns and validate our theory with supportive evidence found in the simulation and experimental data. For the fundamental TE mode which has symmetric E_y field profile, the electromagnetic fields on the wavefront are in the same phase, with the peak field amplitude at the center of the lobe. On the other hand, TE1 mode has two antisymmetric lobes with a field null at the center; two peaks are shifted toward the opposite boundaries, having a phase difference of π. Therefore, to convert a TE0 mode into a TE1 mode, besides the spatial field amplitude rearrangement, the phase of half of the wavefront in the TE0 mode needs to be altered by π with respect to the remaining half wavefront. Additionally, the propagation constant (β) needs to be matched with that of the TE1 mode in the output waveguide. The phase shift can be achieved by introducing a delay to one portion of the wavefront by making it travel a longer optical path. For instance, in the mode exchanger device reported in [29], a narrow trench in the design area splits the TE0 mode wavefront into two parts and, a relative phase shift occurs by having them travel in two imbalanced channels with different effective indices.

For the TE0-TE1 mode converter in this work, Fig. 6(a) suggests that the upper portion of the TE0 mode wavefront travels a longer optical path than the lower portion. This way the upper portion accumulates gradual shifts in the phase and the spatial field amplitude before reaching the

Optics EXPRESS

output waveguide. Thus, across the design area, the fundamental TE mode transforms into TE1 mode with the wavefront having two antisymmetric lobes. This very mechanism is observed also in the field profiles of other TE0-TE1 mode converters we optimized. With the same dimensions of the I/O waveguides, the effective index of TE1 mode is smaller than the effective index of TE0 mode. Therefore, to convert TE0 mode into TE1 mode, the propagation constant needs to be reduced along the x-direction. To accomplish this change in the propagation constant, the optical path deviates from initial propagation axis, adjusting the propagation constant to match that of the TE1 mode in the output waveguide. This explanation also applies to the mode conversion of TE1-TE3. The field pattern in Fig. 6(b) shows both TE1 and TE3 modes have antisymmetric field (E_y) profile with respect to the horizontal axis (black dashed line). To convert the TE1 mode into TE3 mode, two antisymmetric lobes are formed from each of the lobes of TE1 mode. The different portions of the wavefront of TE1 mode travel different optical paths, and a π-phase shift is accumulated on half of each of the TE1 mode lobes. In fact, the field pattern on either side of the horizontal dashed line has strong resemblance with the field pattern observed in Fig. 6(a), implying both TE1 lobes went through identical change in phase and amplitude rearrangements which explains the symmetry in the design geometry. Similar mode conversion mechanisms are demonstrated in [32,33] where tapered waveguides are cascaded to design the MCs having good tolerance to dimensional variations. The (a)symmetry in the design geometry also follows the (a)symmetry in the mode profile and the functionality.

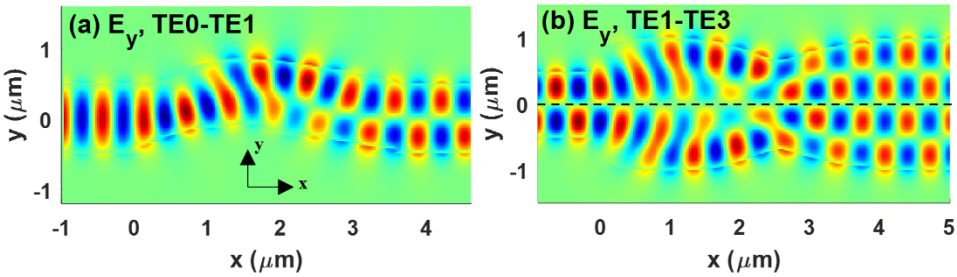

Fig. 6. The y-component of the electric field distribution in (a) TE0-TE1 mode converter and (b) TE1-TE3 mode converter.

The effects of under/over etch on the conversion efficiency in these mode converters provide supportive evidence to the conversion mechanism described above. We observe that the CE peak shifts toward shorter wavelength for over etch fabrication error, where the device boundary shrinks by 10 nm on both sides. The opposite effect is noticed on the CE peak for under etched devices. This shift in the CE peak substantiates the concept of different portions on the wavefront traveling different optical path lengths. As the device boundary shrinks, it favors the optical signal with shorter wavelengths to achieve the peak conversion efficiency, since it requires relatively smaller optical path mismatch (with respect to the central wavelength of 1.55 μm) to accumulate a π-phase shift. A similar argument is applicable to CE peak shift towards longer wavelengths in the under etched devices. We also observe that the CE peaks at shorter wavelengths are higher than those at longer wavelengths. This trend is explained by the fact that optical modes at shorter wavelengths are more confined in the Si waveguide than the modes at longer wavelengths. More confined modes have smaller evanescent field spread in the cladding and better guided by the waveguide. Hence, higher conversion efficiency is obtained at shorter wavelengths. This is consistent with the demonstration in [16] that reduced field overlap with the boundary makes the designs more tolerant to fabrication imperfections.

Optics EXPRESS

3.5. Data transmission experiment

To characterize the time domain performance of the mode converters, 28 Gbps on-off keying (OOK) and 20 GBaud 4-level pulse amplitude modulation (PAM-4) data transmission measurements were carried out. The experimental setup is shown in Fig. 7. Continuous-wave optical power at 1.54 µm from the tunable laser is injected into the $LiNbO_3$ modulator through a polarization controller. 28 Gbps OOK and 20 GBaud PAM-4 electrical signals from the pseudo-random pattern generator (PPG) were used to modulate the optical signal. The modulated optical signal is coupled in and out of the chip using a12-channel single mode optical fiber array. The modulator output power is 0 dBm, and the polarization controller after that introduces an attenuation of ~0.7 dB. Because of the poor coupling efficiency to the grating coupler array, the input power to the EDFA with noise figure below 5 dB (Thorlabs EDFA100S, single mode) is approximately -20 dBm. The EDFA is used to provide a gain of 18 dB. The tunable optical filter is used to suppress the out of band amplified spontaneous emission (ASE) noise of the EDFA. Then the optical signal is sent to a digital communication analyzer to observe the eye diagram. Figure 8(a) shows an open and clear eye diagram of the electrical signal directly coming from the PPG. The eye diagram of the modulator output for PAM-4 signal is open (Fig. 8(b)); the degradation is caused by the RF amplifier. Because of the high system insertion loss around 20 dB at 1.54 µm, the eye quality degrades as the modulated signal travels through the chip, the EDFA, and finally the optical filter.

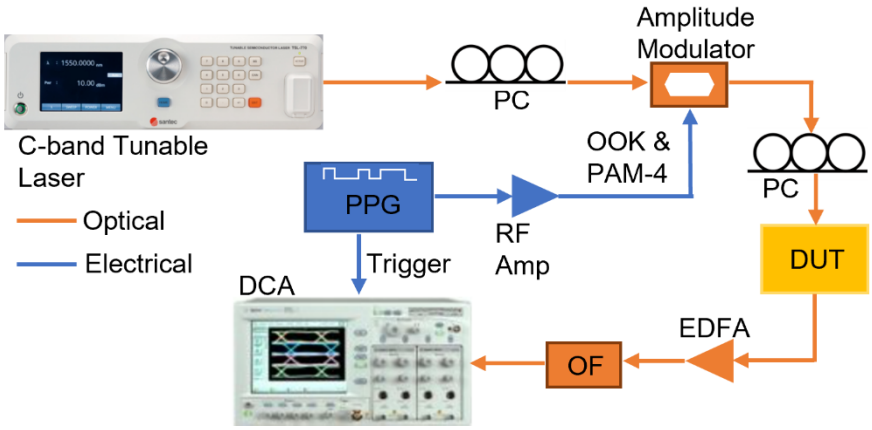

Fig. 7. Experimental setup for 28 Gbps on-off keying (OOK) and 20 Gbd PAM-4 data transmission. PC: polarization controller, DC: bias voltage supply, PPG: pseudorandom pattern generator, RF Amp: RF amplifier, DUT: device under test, EDFA: erbium-doped fiber amplifier, OF: optical filter, DCA: digital communication analyzer.

To identify the noise contributing source. Data transmission is performed afterwards replacing the chip with a variable optical attenuator (VOA) introducing 20 dB attenuation to mimic the insertion loss of the grating couplers. For OOK signal, the Q-factor of the modulator output signal is 8.41 dB, while for TE0-TE1 and TE1-TE3 MCs, we observe open eye diagrams with a Q-factor of 8.01 dB and 7.97 dB, respectively. Replacing the chip with VOA also results in OOK transmission with a Q-factor of 8 dB, implying that the SNR degradation is due to the ASE noise of the EDFA.

Optics EXPRESS

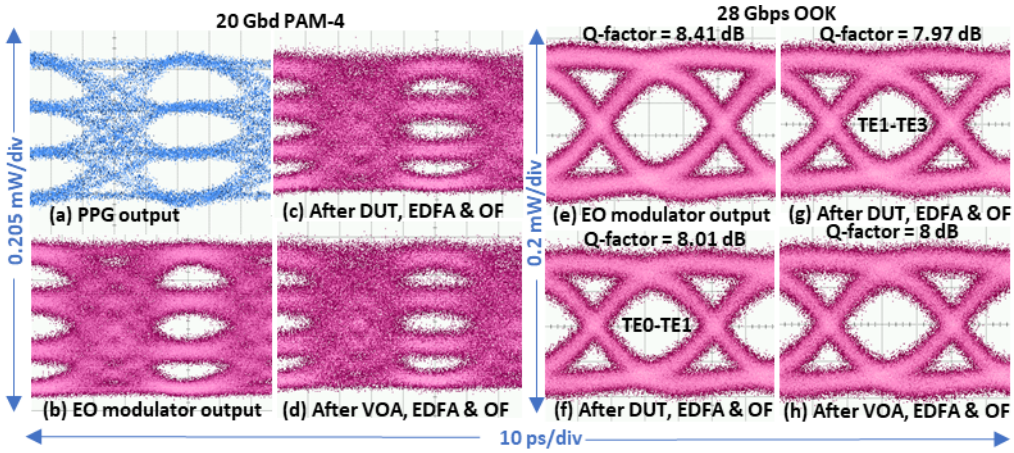

Fig. 8. (a) Eye diagrams of the 20 GBaud PAM-4 electrical signal coming from the pseudorandom pattern generator, eye diagram of the optical signal: (b) the optical modulator output, (c) after going through the chip and being amplified 18 dB by the EDFA and filtered by an optical filter, (d) when the chip was replaced by a variable optical attenuator, Eye diagrams for 28 Gbps OOK signal transmission: (e) the optical modulator output, (f) after going through the TE0-TE1 mode converter, EDFA, and optical filter, (h) when the chip was replaced by the VOA (variable optical attenuator).

4. Conclusion

We report inverse designed broadband SOI mode converters for TE polarization using adjoint shape optimization. The same method can be used to design mode converters for TM polarization by carefully selecting the mode order in the optimization algorithm. The footprints of the MCs in this work range from 3 μm to 7.8 μm in length. The mode conversion efficiencies are predicted to be above 95% across 100 nm wavelength span centered at 1.55 μm based on 3D FDTD simulations. Experimental data shows the maximum insertion loss is 1.2 dB across the wavelength range from 1.5 μm to 1.58 μm, while their modal crosstalks are below -19 dB in the C-band. Due to the bandwidth limitation of the grating couplers used for interfacing with fibers, we deem the measured results beyond 1.58 μm unreliable and therefore are not reported. The design approach is formulated in such a way that the device structure consists of a single silicon block between the I/O waveguides, ensuring high confinement of the optical fields in Si core, which makes the designs robust to fabrication imperfections. Despite introducing ±20 nm waveguide width variations, the mode conversion efficiency remains above 90% across the entire bandwidth of 100 nm. We also analyze the working mechanism of the MCs and validate it with simulation and experimental data. We obtain open eye diagrams for 28 Gbps OOK transmission with a Q-factors of 8 dB and a 20 GBaud PAM-4 payload transmission, demonstrating the utility of these devices in high-capacity optical communication systems.

Funding. National Research Council Canada.

Acknowledgments. The authors thank Dusan Gostimirovic for his support through technical discussions while conducting this research.

Disclosures. The authors declare that there are no conflicts of interest related to this article.

Data availability. Data underlying the results presented in this paper are not publicly available at this time but may be obtained from the authors upon reasonable request.

Optics EXPRESS

References

1. H. Jia, L. Zhang, J. Ding, L. Zheng, C. Yuan, and L. Yang, "Microring modulator matrix integrated with mode multiplexer and de-multiplexer for on-chip optical interconnect," Opt. Express **25**(1), 422–430 (2017).
2. B. Stern, X. Zhu, C. P. Chen, L. D. Tzuang, J. Cardenas, K. Bergman, and M. Lipson, "On-chip mode-division multiplexing switch," Optica **2**(6), 530–535 (2015).
3. D. Vercruysse, N. V. Sapra, K. Y. Yang, and J. Vučković, "Inverse-Designed Photonic Crystal Circuits for Optical Beam Steering," ACS Photonics **8**(10), 3085–3093 (2021).
4. J. Lu and J. Vučković, "Objective-first design of high-efficiency, small-footprint couplers between arbitrary nanophotonic waveguide modes," Opt. Express **20**(7), 7221–7236 (2012).
5. R. Xiao, Y. Shi, J. Li, P. Dai, Y. Zhao, L. Li, J. Lu, and X. Chen, "On-chip mode converter based on two cascaded Bragg gratings," Opt. Express **27**(3), 1941–1957 (2019).
6. M. Soljačić, S. G. Johnson, S. Fan, M. Ibanescu, E. Ippen, and J. D. Joannopoulos, "Photonic-crystal slow-light enhancement of nonlinear phase sensitivity," J. Opt. Soc. Am. B **19**(9), 2052–2059 (2002).
7. Z. He, H. Li, S. Zhan, B. Li, Z. Chen, and H. Xu, "Tunable multi-switching in plasmonic waveguide with Kerr nonlinear resonator," Sci. Rep. **5**(1), 1–5 (2015).
8. A. Mahigir, P. Dastmalchi, W. Shin, S. Fan, and G. Veronis, "Plasmonic coaxial waveguide-cavity devices," Opt. Express **23**(16), 20549–20562 (2015).
9. Z. Zhang, X. Hu, and J. Wang, "On-chip optical mode exchange using tapered directional coupler," Sci. Rep. **5**(1), 1–5 (2015).
10. M. Ye, Y. Yu, C. Sun, and X. Zhang, "On-chip data exchange for mode division multiplexed signals," Opt. Express **24**(1), 528–535 (2016).
11. J. Lu and J. Vučković, "Nanophotonic computational design," Opt. Express **21**(11), 13351–13367 (2013).
12. C. M. Lalau-Keraly, S. Bhargava, O. D. Miller, and E. Yablonovitch, "Adjoint shape optimization applied to electromagnetic design," Opt. Express **21**(18), 21693–21701 (2013).
13. J. S. Jensen and O. Sigmund, "Topology optimization of photonic crystal structures: a high-bandwidth low-loss T-junction waveguide," J. Opt. Soc. Am. B **22**(6), 1191–1198 (2005).
14. D. Sell, J. Yang, S. Doshay, R. Yang, and J. A. Fan, "Large-angle, multifunctional metagratings based on freeform multimode geometries," Nano Lett. **17**(6), 3752–3757 (2017).
15. L. H. Frandsen, Y. Elesin, L. F. Frellsen, M. Mitrovic, Y. Ding, O. Sigmund, and K. Yvind, "Topology optimized mode conversion in a photonic crystal waveguide fabricated in silicon-on-insulator material," Opt. Express **22**(7), 8525–8532 (2014).
16. G. Zhang, D. Xu, Y. Grinberg, and O. Liboiron-Ladouceur, "Topological inverse design of nanophotonic devices with energy constraint," Opt. Express **29**(8), 12681–12695 (2021).
17. H. Jia, T. Zhou, X. Fu, J. Ding, and L. Yang, "Inverse-design and demonstration of ultracompact silicon meta-structure mode exchange device," ACS Photonics **5**(5), 1833–1838 (2018).
18. W. Chang, L. Lu, X. Ren, D. Li, Z. Pan, M. Cheng, D. Liu, and M. Zhang, "Ultra-compact mode (de) multiplexer based on subwavelength asymmetric Y-junction," Opt. Express **26**(7), 8162–8170 (2018).
19. C. Dory, D. Vercruysse, K. Y. Yang, N. V. Sapra, A. E. Rugar, S. Sun, D. M. Lukin, A. Y. Piggott, J. L. Zhang, M. Radulaski, and K. G. Lagoudakis, "Inverse-designed diamond photonics," Nat. Commun. **10**(1), 3309 (2019).
20. M. M. Masnad, D. Xu, Y. Grinberg, and O. Liboiron-Ladouceur, "Computationally efficient and fabrication error tolerant inverse-designed mode converters," *IEEE Photonics Conference (IPC)* 1–2 (2021).
21. D. Vercruysse, N. V. Sapra, L. Su, R. Trivedi, and J. Vučković, "Analytical level set fabrication constraints for inverse design," Sci. Rep. **9**(1), 8999 (2019).
22. V. Liu, D. A. B. Miller, and S. Fan, "Ultra-compact photonic crystal waveguide spatial mode converter and its connection to the optical diode effect," Opt. Express **20**(27), 28388–28397 (2012).
23. M. M. Masnad, Y. Grinberg, D. Xu, and O. Liboiron-Ladouceur, "Physics-guided Inverse Design for SiPh Mode Manipulation," *OSA Photonics in Switching and Computing*, Tu4A-4 (2021).
24. Refractive index database. https://refractiveindex.info/.
25. C. Zhu, R. H. Byrd, P. Lu, and J. Nocedal, "Algorithm 778: L-BFGS-B: Fortran subroutines for large-scale bound-constrained optimization," ACM Trans. Math. Softw. **23**(4), 550–560 (1997).
26. Ansys Lumerical Photonics Simulation & Design Software. https://www.ansys.com/products/photonics.
27. Lumerical Support- Inverse design of y-branch. https://support.lumerical.com/hc/en-us/articles/360042305274-Inverse-design-of-y-branch.
28. Y. Ding, J. Xu, F. D. Ros, B. Huang, H. Ou, and C. Peucheret, "On-chip two-mode division multiplexing using tapered directional coupler-based mode multiplexer and demultiplexer," Opt. Express **21**(8), 10376–10382 (2013).
29. G. Zhang and O. Liboiron-Ladouceur, "Scalable and low crosstalk silicon mode exchanger for mode division multiplexing system enabled by inverse design," IEEE Photonics J. **13**(2), 1–13 (2021).
30. C. Williams, G. Zhang, R. Priti, G. Cowan, and O. Liboiron-Ladouceur, "Modal crosstalk in Silicon photonic multimode interconnects," Opt. Express **27**(20), 27712–27725 (2019).
31. Z. Lu, J. Jhoja, J. Klein, X. Wang, A. Liu, J. Flueckiger, J. Pond, and L. Chrostowski, "Performance prediction for silicon photonics integrated circuits with layout-dependent correlated manufacturing variability," Opt. Express **25**(9), 9712–9733 (2017).

Optics EXPRESS

32. D. Chen, X. Xiao, L. Wang, W. Liu, Q. Yang, and S. Yu, "Low-loss and fabrication tolerant silicon mode-order converters based on novel compact tapers," Opt. Express **23**(9), 11152–11159 (2015).
33. D. Chen, X. Xiao, L. Wang, W. Liu, Q. Yang, and S. Yu, "Highly efficient silicon optical polarization rotators based on mode order conversions," Opt. Lett. **41**(5), 1070–1073 (2016).